Defining Shape Measures for 3D Star-Shaped Particles: Sphericity, Roundness, and Dimensions[1]

Jeffrey W. Bullard, Edward J. Garboczi

Materials and Structural Systems Division, National Institute of Standards and Technology, Gaithersburg, Maryland USA 20899-8615

Abstract

Truncated spherical harmonic expansions are used to approximate the shape of 3D star-shaped particles including a wide range of axially symmetric ellipsoids, cuboids, and over 40 000 real particles drawn from seven different material sources. This mathematical procedure enables any geometric property to be calculated for these star-shaped particles. Calculations are made of properties such as volume, surface area, triaxial dimensions, the maximum inscribed sphere, and the minimum enclosing sphere, as well as differential geometric properties such as surface normals and principal curvatures, and the values are compared to the analytical values for well-characterized geometric shapes. We find that a particle's Krumbein triaxial dimensions, widely used in the sedimentary geology literature, are essentially identical numerically to the length, width, and thickness dimensions that are used to characterize gravel shape in the construction aggregate industry. Of these dimensions, we prove that the length is a lower bound on a particle's minimum enclosing sphere diameter and that the thickness is an upper bound on its maximum inscribed sphere diameter. We examine the "true sphericity" and the shape entropy, and we also introduce a new sphericity factor based on the radius ratio of the maximum inscribed sphere to the minimum enclosing sphere. This bounding sphere ratio, which can be calculated numerically or approximated from macroscopic dimensions, has the advantage that it is less sensitive to surface roughness than the

[1]Powder Technol., 249 (2013) 241–252

true sphericity. For roundness, we extend Wadell's classical 2D definition for particle silhouettes to 3D shapes and we also introduce a new roundness factor based on integrating the dot product of the surface position unit vector and the unit normal vector. Limited evidence suggests that the latter roundness factor more faithfully captures the common notion of roundness based on visual perception of particle shapes, and it is significantly simpler to calculate than the classical roundness factor.
Key words: granular materials, particle shape, numerical modeling

1. Introduction

Particle shape influences the microscale behavior and macroscopic properties of granular media, including the polarizability [1], the intrinsic viscosity [1, 2], and settling velocities [3, 4] of particles in suspension. Conductivity and rigidity percolation thresholds, as well as maximum packing fractions, are extremely sensitive to the particle shape [5, 6], and the effective properties of granular composites can be significantly influenced by inclusion shape when the contrast between the corresponding properties of the inclusion and matrix phases is high. By implication, a better characterization and understanding of particle shape could lead to improved understanding and control of the behavior of a wide range of natural and synthetic materials, including soils, biomineral composites, slurries, food products, construction materials like gravel, sand, and cement, pharmaceutical powders, glass beads used in pavement coating paints to enhance retroreflectivity, and flammable dusts produced by various industrial processes.

Probably the most basic characteristic of an object's shape is the relation between its surface area and its volume. All 3D Euclidean objects have a 2/3 power law scaling between their surface

Email addresses: `jeffrey.bullard@nist.gov` (Jeffrey W. Bullard), `edward.garboczi@nist.gov` (Edward J. Garboczi)

area and volume,

$$A = \beta V^{2/3} \tag{1}$$

where β depends on shape and is often called the scaling factor. A sphere has $\beta_s = (36\pi)^{1/3} \approx 4.836$, where the subscript "s" denotes the value for a sphere. By the isoperimetric inequality [7], for the surface area of a sphere, β_s is the minimum possible value of the scaling factor for any 3D Euclidean object.

The scaling factor is useful but as a single parameter it does not provide much information about other common indicators of shape such as aspect ratio or the sharpness of edges and corners. In his work on sediments, Hakon Wadell [8] was the first to propose decomposing shape descriptions into the two distinct factors of *sphericity* and *roundness*. Sphericity indicates how equiaxed the particle is, and is the opposite of anisometry or ellipticity. Roundness gives information about how blunted or rounded the corners and edges of the particle are, and is the opposite of angularity. Wadell's definition of a particle's sphericity is

$$S_W = \frac{A_s}{A} \tag{2}$$

where A is the particle's surface area and A_s is the surface area of a sphere having the same volume. From Eq. (1), one may easily demonstrate that $S_W = \beta_s/\beta$. Again, by the isoperimetric inequality, $0 < S_W \leq 1$, with the upper bound of unity being attained only by a sphere. Table I shows values of S_W for the five Platonic solids and two prolate ellipsoids. S_W does correspond roughly with one's common sense of the approximation of the object to a sphere (e.g., a cube is less spherical than an icosahedron but more spherical than a tetrahedron).

A possible complication in using S_W, although not evident from the table, is its dependence on the length scale of surface roughness; objects with a spherical macroscopic shape but which have significant roughness or planar faceting at the microscopic or nanoscopic scale will have S_W values that depend on the resolution with which the surface area is measured [9]. This disadvantage might be remedied by defining an alternative measure of sphericity based on the ratio of the object's bounding spheres,

$$S_{BS} = \frac{\rho_{\mathrm{is}}}{\rho_{\mathrm{es}}} \tag{3}$$

where ρ_{is} and ρ_{es} are the radius of the maximum inscribed sphere and of the minimum enclosing sphere, respectively, so that $0 < S_{BS} \leq 1$. This alternative sphericity measure characterizes the thinnest (non-concentric) spherical shell within which the particle surface can fit, and $S_{BS} = 1$ only for a sphere.

Since Wadell's classification of sphericity, a variety of other sphericity factors have been proposed that attempt to capture the same idea in terms of the uniformity of the particle dimensions or of the projected area [10, 11, 12, 13, 3]. Most of these utilize the so-called triaxial dimensions of the particle, $D_1 \geq D_2 \geq D_3$. D_1 is the length of the longest line segment that can be drawn between any two surface points. D_2 is the longest dimension of the maximum projected area of the particle that is also perpendicular to D_1, and D_3 is the longest dimension perpendicular to both D_1 and D_2. [14]. Among the shape factors proposed, the Hofmann shape entropy [13] has attracted attention recently for its ability to correlate with particle settling velocity [3, 4] and with cognitive perception of shape [15]:

$$S_H = \frac{1}{\ln(1/3)} \sum_{i=1}^{3} p_i \ln p_i \tag{4}$$

where

$$p_i \equiv \frac{D_i}{D_1 + D_2 + D_3}$$

$S_H = 1$ if all three triaxial dimensions are equal, and it decreases to zero as one dimension becomes much different than the other two.

Table I catalogs S_H for the same geometric objects considered earlier. S_H ranks the two ellipsoids in the same order as both S_W and S_{BS}, although the values themselves are significantly greater. However, the five platonic solids are not well differentiated by S_H because $S_H \geq 0.989$ for all of them and, in fact, the regular octahedron has a slightly higher value than either the dodecahedron or the icosahedron.

Procedures for measuring $\{D_1, D_2, D_3\}$ of rocks have been published [14], and methods for estimating the surface area of rocks by painting or foil wrapping have been proposed [16]. We note that a slightly different set of dimensions, $\{L, W, T\}$ is often used to characterize the shape of aggregate particles in the construction industry. L is the particle's longest axis and is equal to D_1. W is the longest axis perpendicular to L and need not bear any relation to the maximum projected area. D_2 must also be perpendicular to L but is constrained to lie in the plane of maximum projected area, so $D_2 \leq W$. Finally, T is the longest axis that is perpendicular to both L and W. Measurement of $\{L, W, T\}$ for gravel has been standardized in ASTM D 4791 [17, 18]. The relationships between D_2 and W, and between D_3 and T, will be examined more closely in the Results and Discussion section.

Aside from sphericity factors, Wadell [8] also defined the "roundness" as a distinct shape property. His definition requires knowledge of the radius of curvature of the "corners" observed in three different 2D projections of the particle that are at right angles to each other. He further defined a corner as "every such part of the outline of an area (projection area) which has a radius of curvature equal to or less than the radius of curvature of the maximum inscribed circle of the same area." [8]. With this definition of a corner, Wadell's definition of roundness of a given projection is

$$R_W = \frac{\sum_{i=1}^{N} |\rho_i|}{N\rho_{\mathrm{ic}}} \tag{5}$$

where the sum is taken over all the N corners of the projection, ρ_i is the radius of curvature of the i-th corner, and ρ_{ic} is the radius of the largest circle that can be inscribed in the section. A corner is any part of the surface with $\rho_i < \rho_{\mathrm{ic}}$, so dividing by ρ_{ic} ensures that the maximum possible roundness is one. Note that corners and edges on fully faceted objects have $\rho = 0$, so R_W of any projection through a polyhedron is always zero. Wadell stated that roundness is intrinsically a property of 2D cross sections of a particle instead of the particle itself, and that two or more mutually perpendicular planar sections should be sampled to achieve an accurate measurement of roundness of a given particle. However, this statement may have been motivated primarily by a measurement problem at the time instead of any fundamental geometric consideration: any point on the surface of a 3D particle has two principal radii of curvature, and the experimental measurement of these two radii is generally a difficult task for arbitrary particle shapes.

Until recently, sphericity factors based on $\{D_1, D_2, D_3\}$ or on $\{L, W, T\}$ have received more attention in the literature than roundness factors due to the relative simplicity of the measurements for sphericity. A more complete 3D shape characterization of particles ranging in size from micrometers to centimeters has been difficult to achieve. However, the increasingly widespread accessibility of lab-scale micro-computed tomography (μCT) has made possible the acquisition of 3D images of collections of tens of thousands of particles. Particles are dispersed in a sample in some way (e.g., hardened in epoxy) and then scanned. Image processing software extracts individual particles from the dispersion and numerical methods are used to construct a spherical harmonic series approximation of the particle surface. Using this series, any surface or volume integral can be evaluated using standard quadrature, and any algorithm that involves the internal or surface coordinates of the particle can be performed. This allows detailed numerical analysis of particle shape [19, 20, 21].

In this paper, we use these same methods to analyze macroscopic and differential geometric properties of particle shapes, including the volume, surface area, triaxial dimensions, maximum inscribed sphere and minimum enclosing sphere (hereafter called the bounding spheres for convenience), and several sphericity and roundness factors, some of which appear to be new. With access to the full 3D shape, one can compute not only the exact 3D analog of the shape factors already described, but one can also visualize and quantify the contributions of different surface features to these shape factors. The next section briefly reviews the spherical harmonic representation of 3D particle shape and the differential geometric concepts for measuring local surface properties. We will apply the analysis first to simple geometric objects like those in Table I and then to representations of individual particles drawn from real granular media populations, developing an estimate of the statistical distribution of different shape factors among the different populations.

2. Mathematical Shape Characterization

2.1. Spherical Harmonic (SH) Expansions

A truncated spherical harmonic (SH) series provides a convenient way to characterize the surface of a star-shaped 3D object. An object is star-shaped if there is a fixed point, O, in its interior for which a straight line drawn from that point to any other point inside the object lies entirely within the object. The collection of all such starting points itself forms a convex set and is often called the kernel of the star-shaped object. The star-shaped requirement will exclude from consideration particles with overhangs or internal voids, but most inorganic particles that are produced by manufacturing processes such as grinding are star-shaped. These are the only kind considered in this paper. If we place the fixed point O of the particle at the origin of a spherical polar coordinate system with polar coordinate θ and azimuthal coordinate ϕ, the distance of any point on the surface from the origin is a single-valued function, $r(\theta, \phi)$, and this function can be approximated as a truncated SH series,

$$r(\theta, \phi) \approx \sum_{n=0}^{N} \sum_{m=-n}^{n} a_{nm} Y_{nm}(\theta, \phi) \tag{6}$$

with the approximation being exact in the limit $N \to \infty$. The SH series representation is powerful because it is analytic; once constructed for a particle, any linear dimension of the particle can be determined, including the triaxial dimensions. More importantly, any integral on the particle surface or its interior, or any differential quantity along the surface, can be set up analytically and evaluated numerically [18, 21].

A well-known artifact introduced by truncated SH series representations is the Gibbs phenomenon, or "ringing"—the appearance of small, high-frequency ripples on the surface and especially near the poles. However, a common technique for reducing the ringing artifact, without significantly affecting the overall shape, is to filter the series with the so-called Lanczos sigma factor [22], by which each of the SH coefficients a_{nm} are transformed according to[2]

$$a'_{nm} = a_{nm}\,\mathrm{sinc}\left(\frac{(n-n_0)\pi}{N-n_0}\right) , \qquad (n_0 \leq n \leq N) \tag{7}$$

where $\mathrm{sinc}(x) \equiv (\sin x)/x$ and n_0 is the degree below which the coefficients remain unchanged and N is the cutoff degree in Eq. (6). The Lanczos sigma factor progressively reduces the magnitude of the SH coefficients as n approaches the cutoff frequency. The Results and Discussion section includes some demonstrations of the effectiveness of this approach in reducing surface noise caused by ringing.

2.2. 3D Shape Descriptors

2.2.1. Dimensions and Sphericity

From its SH series approximation, $r(\theta, \phi)$, a particle's triaxial dimensions can be approximated using a sequence of numerical searches in (θ, ϕ) space, whereby the maximum dimension of the particle (D_1) is first found by a two-step search [18]. A collection of points is decorated on the surface, and vectors are constructed between each pair of points. The longest of these vectors is chosen as a coarse approximation of D_1. The search for a longer vector is then refined using a denser collection of points in a neighborhood of the head and tail of this vector. The longest vector found, $\vec{d_1}$, has a magnitude $|\vec{d_1}| = D_1$. The triaxial width (D_2) is then found by the following procedure. First, the particle is rotated through the three standard Euler angles (α, β, γ) such that $\vec{d_1}$ is parallel to the x-axis. The following steps are then performed iteratively: (1) the particle's projected area onto the xy-plane is calculated by Gaussian quadrature; (2) the longest vector $\vec{d_2}$ perpendicular to $\vec{d_1}$ for this projected area is found by a search over all pairs (x_i, y_i) and (x_i, y_j) of

[2]The sigma factor used here is trivially more general than the sigma factor as defined by Lanczos, which does not have a lower threshold n_0.

quadrature points on the perimeter having equal x values; (3) the particle is incrementally rotated about the x-axis, and then steps (1) and (2) are repeated. After sampling all projected areas, the vector $\vec{d_2}$ associated with the maximum projected area is selected and $D_2 = |\vec{d_2}|$. Finally, the triaxial thickness (D_3) is found by performing another search over all pairs of surface points, constructing a vector $\vec{d_3}$ between each pair and selecting the longest one that is orthogonal both to $\vec{d_1}$ and to $\vec{d_2}$. The orthogonality condition is enforced by requiring $\hat{d}_i \cdot \hat{d}_{j \neq i} < 0.1$, where $\hat{d}_i \equiv \vec{d_i}/|\vec{d_i}|$ and the inequality ensures that the vectors are mutually perpendicular to within 5°.

The dimensions $\{L, W, T\}$ described in the previous section are found by a somewhat simpler procedure because the maximum projected area is not involved. The length vector $\vec{l} = \vec{d_1}$ and $L = D_1$. W is found by searching the remaining vectors, using the same kind of two-step search, for the longest one $\vec{w}$ that is also perpendicular to $\vec{l}$ (that is, $\hat{w} \cdot \hat{l} < 0.1$), and $W = |\vec{w}|$. Finally, T is found by the same two-step search and choosing the longest remaining vector $\vec{t}$ that is perpendicular to within 3° to 5° to both $\vec{w}$ and $\vec{l}$, and $T = |\vec{t}|$. The values obtained are within the uncertainty in measurements on rocks using a standard method (ASTM D4791) [18]. These dimensions can be useful in developing approximate formulas for volume and surface area, and for approximating particles as either rectangular parallelipipeds or triaxial ellipsoids [18].

The Hofmann shape entropy can be calculated directly from the triaxial dimensions according to Eq. (4). Wadell's sphericity definition in Eq. (2) requires knowledge of the particle's volume and surface area, but these also can be calculated from $r(\theta, \phi)$:

$$V = \frac{1}{3} \int_0^{2\pi} \mathrm{d}\phi \int_0^{\pi} r^3 \sin(\theta) \, \mathrm{d}\theta \tag{8}$$

$$A = \int_0^{2\pi} \mathrm{d}\phi \int_0^{\pi} r \sqrt{r_\phi^2 + \left(r^2 + r_\theta^2\right) \sin^2(\theta)} \, \mathrm{d}\theta \tag{9}$$

where r_θ and r_ϕ are the derivatives of r with respect to θ and ϕ, respectively; formulas for the derivatives in terms of spherical harmonics are given elsewhere [19].

2.2.2. Roundness

Wadell's definition of roundness in Eq. (5) requires knowledge of the radius of curvature of each "corner" observed on the perimeter of a 2D projection of the particle. To formulate an equivalent 3D roundness factor, it will be helpful to start by recasting Wadell's definition in 2D as an integral over the perimeter P of the cross section:

$$R_W = \frac{\rho_{\mathrm{ic}}^{-1} \displaystyle\int_P |\rho|\, f(\rho)\, \mathrm{d}P}{\displaystyle\int_P f(\rho)\, \mathrm{d}P} \tag{10}$$

$$f(\rho) = \begin{cases} 1 & \text{if } |\rho| \leq \rho_{\mathrm{ic}} \\ 0 & \text{if } |\rho| > \rho_{\mathrm{ic}} \end{cases} \tag{11}$$

In principle, this latter definition can be extended to 3D, using the radius ρ_{is} of the maximum inscribed sphere within the particle and integrating over the surface area. However, a unique measure of curvature does not exist on surfaces as it does for curves. Instead, the radius of curvature measured at a point depends on the path through the point along which the measurement is made. If the radius of curvature is the same for every path through a point, that point is called an umbilic point. Otherwise, a fundamental result of differential geometry is that, of all the different values of the radius of curvature through a point, the maximum value ρ_{max} and the minimum value ρ_{min} are found along paths that are perpendicular to each other. These two perpendicular paths are called the *principal directions* at the point, and the inverses $\kappa_{\mathrm{max}} = 1/\rho_{\mathrm{min}}$ and $\kappa_{\mathrm{min}} = 1/\rho_{\mathrm{max}}$ are the *principal curvatures* at the point [23]. To illustrate, every point on a sphere of radius R is an umbilic with $\kappa = 1/R$ and every point on a planar section, such as the face of a cube, is an umbilic with $\kappa = 0$. Along a slightly rounded edge joining two planar sections (*e.g.*, a blunted cube edge), one of the principal directions lies along the edge, the other is perpendicular to it, and $\kappa_{\mathrm{max}} \to \infty$ as the edge becomes sharper while $\kappa_{\mathrm{min}} = 0$. Curvature is undefined at non-differentiable features such as perfectly sharp edges and corners of polyhedra. Finally every point on the side wall of a right circular cylinder with radius R_{cyl} has $\kappa_{\mathrm{max}} = 1/R_{\mathrm{cyl}}$ and $\kappa_{\mathrm{min}} = 0$. The appendix to Ref. [19] provides the differential geometric relations that are required to compute the principal directions and curvatures at a point using the SH representation.

With these considerations in mind, among all the possible functions of κ_{max} and κ_{min} that could be used to characterize the curvature of a surface point, the one that seems closest in spirit to Wadell's 2D definition is simply $|\kappa_{\mathrm{max}}^{-1}|$. We choose an absolute value because a surface with more than one positive curvature "peak" on it will also contain at least one negative curvature "valley". Therefore, our 3D analog of Wadell's definition of roundness is

$$R_W = \frac{\kappa_{\mathrm{is}} \displaystyle\int_A f(\kappa)\, |\kappa_{\mathrm{max}}|^{-1}\, \mathrm{d}A}{\displaystyle\int_A f(\kappa)\, \mathrm{d}A} \tag{12}$$

$$f(\kappa) = \begin{cases} 1 & \text{if } |\kappa_{\mathrm{max}}| \geq \kappa_{\mathrm{is}} \\ 0 & \text{if } |\kappa_{\mathrm{max}}| < \kappa_{\mathrm{is}} \end{cases} \tag{13}$$

The full form of Eq. (12) in spherical polar coordinates is

$$R_W = \frac{\kappa_{\mathrm{is}} \displaystyle\int_0^{2\pi} \mathrm{d}\phi \int_0^{\pi} f(\kappa)\, |\kappa_{\mathrm{max}}|^{-1}\, r \sqrt{r_\phi^2 + \left(r^2 + r_\theta^2\right)\sin^2(\theta)}\; \mathrm{d}\theta}{\displaystyle\int_0^{2\pi} \mathrm{d}\phi \int_0^{\pi} f(\kappa)\, r \sqrt{r_\phi^2 + \left(r^2 + r_\theta^2\right)\sin^2(\theta)}\; \mathrm{d}\theta} \tag{14}$$

Eq. (14) captures the spirit of Wadell's original definition of roundness by considering only those portions of a particle surface that can be classified as edges or corners. However, we propose an alternative definition of roundness that (1) includes the entire surface, (2) does not require a separate calculation of the maximum inscribed sphere, and (3) does not require calculation of principal curvatures. This third point is important because surface curvatures, requiring the calculation of second derivatives, are harder to compute. As we consider later, surface curvature calculations are also much more sensitive to surface ringing than are volume and surface area. This alternative considers only the angle between the surface position vector $\vec{r}(\theta, \phi)$ and the unit normal vector to the surface $\hat{n}(\theta, \phi)$. Fig. 1 shows the general idea for two different portions of a surface. Relatively flat regions of a particle surface separated by highly curved edges or corners are associated with large angles between $\vec{r}$ and $\hat{n}$, while smoothly rounded portions tend to have smaller angles between these two vectors. The angle can be quantified by the dot product $\hat{r} \cdot \hat{n}$, where $\hat{r} = \vec{r}/|\vec{r}|$, so we define an alternative measure of 3D roundness as

$$R_n = \frac{\displaystyle\int_A |\hat{r} \cdot \hat{n}| \, \mathrm{d}A}{\displaystyle\int_A \mathrm{d}A} \tag{15}$$

The divergence theorem guarantees that R_n is independent of the choice of the origin for defining $\hat{r}$ as long as the origin belongs to the convex set of points with respect to which the particle is star-shaped. R_n has the same bounds as R_W, that is, $0 < R_n \leq 1$. Also, like R_W, $R_n = 1$ only for a sphere.

3. Results

3.1. Numerical Considerations

Evaluation of a particle's volume, area, and roundness, according to Eqs. (8), (9), and (12) is accomplished by discretizing the (θ, ϕ)-space of a spherical polar coordinate system onto a mesh of (θ, ϕ) pairs, chosen by using the Gaussian points in a Gaussian quadrature. In addition, we also evaluate the triaxial dimensions of particles, as well as the maximum inscribed sphere, by straightforward searches in the same discretized space. The results will generally depend on the fineness of the discretization, on the cutoff degree N used to truncate the SH expansion, and on the application of the Lanczos sigma factor, Eq. (7), to reduce the effects of ringing. Therefore, we begin by examining the sensitivity of the results to these factors, using as a representative shape a prolate ellipsoid with a 5:1 aspect ratio.

Fig. 2 shows how the calculated volume and surface area of a 5:1 prolate ellipsoid converge to values close to their true values as the cutoff degree N increases. In these calculations, the number of Gaussian quadrature points was fixed at $22,500$ (i.e., 150^2) and the sigma factor was not applied. Both the volume and surface area are within 2 % of their true values for $N \geq 10$, and the errors are reduced to < 0.5 % for $N \geq 20$. Accuracy is also influenced by the number of quadrature points used to evaluate the integrals, although the integrals converge rapidly with increasing numbers of quadrature points. Fig. 3 shows that for the same ellipsoid, this time approximated with $N = 60$, accuracy greater than 0.01 % in both volume and surface area can be achieved by using as few as 256 total quadrature points. These two figures clearly show that the accuracy of the shape representation (i.e., the cutoff degree of the expansion) is much more important for the accuracy of the volume and surface area than is the number of Gaussian quadrature points used. The trends shown in these plots are qualitatively general, although the actual accuracies depend on the shape of the object and on the distribution of the quadrature points in (θ, ϕ)-space.

When calculating principal curvatures on a particle surface, the ringing artifact can significantly affect the results; artificial ripples produced by truncating the SH series can have appreciable curvatures even though their amplitude is small. However, the effect of ringing and its correction has little effect on the volume and surface area calculations. Fig. 4 shows the computed volume and surface area when each SH coefficient having degree $n \geq n_0$ is filtered with the Lanczos sigma factor. For the mesh used in these calculations, Fig. 4 indicates that the sigma factor degrades the accuracy only when $n_0 < 10$, with a maximum error of about 1 % occurring when $n_0 = 0$. The data in Fig. 4 were obtained for a prolate 5:1 ellipsoid using $N = 30$, but qualitatively equivalent results are obtained for an oblate 1:0.1 ellipsoid and for a rounded cube, and using either $N = 30$ or $N = 60$.

The sigma factor has a much greater effect on the calculated distribution of principal curvatures on a surface than it does on the calculated values of the volume and surface area. Fig. 5 shows the values of the principal curvatures for an SH approximation of a 5:1 prolate ellipsoid, truncated at $N = 30$, along a constant-ϕ path from $\theta = 0°$ (the north pole) to $\theta = 90°$ (the equator). The circular and square points are values calculated without and with the application of the sigma factor, respectively, and the dashed curves are the true principal curvatures calculated using the exact equation for the ellipsoid. The numerical values in Fig. 5, with or without the sigma factor, overestimate the true curvature of the ellipsoid for $\theta < 15°$ because the truncation of the SH series for a prolate ellipsoid causes a slight blunting of the ellipsoid's tips at the north and south poles. This error could be improved by using higher cutoff values in the SH expansion. The larger principal curvature is much more accurate at $\theta > 30°$. However, without applying the sigma factor, the lower principal curvature begins to oscillate with an increasing amplitude; this is a characteristic ringing effect, and the plot shows that applying the sigma factor reduces the oscillations significantly. When one looks closely at the ellipsoid shape without correction, the ringing effect looks like surface ripples oriented normal to the ellipsoid's principal axis, and produces the effect seen in Fig. 5.

Although the calculated curvatures of an ellipsoid can be influenced considerably by ringing artifacts when they are not dampened by the sigma factor, the effects are even more pronounced on particles with large flat areas, such as the faces of a cube. Fig. 6 shows the SH expansion of a cube truncated at $N = 30$. Without the sigma factor (left image), the cube faces have a pronounced rippling pattern. With the sigma factor (right image), the ripples are again reduced significantly, although the edges and corners are noticeably blunter. The quantitative influences on the principal curvatures are shown in Fig. 7, which plots the principal curvatures along a constant-ϕ path from $\theta = 0°$ (center of the upper face) to $\theta = 90°$ (center of the front face). For an exact cube, one principal curvature along this path is zero, and the other principal curvature is a δ-function centered at 45°. Again, without the sigma factor (circles), both curvatures oscillate significantly around zero. One of the principal curvatures increases to a maximum of about 23 at the cube edge. As indicated by the image of the shapes, the application of the sigma factor reduces the curvature oscillations significantly on the faces. The maximum deviation from the true value of zero is only about 0.2, although the maximum curvature at the edge is also reduced to only 65 % of the value obtained without the sigma factor. However, this tradeoff is probably acceptable for calculating R_W because the edges and corners occupy less surface area than the flat faces; the large oscillations in the maximum principal curvature on the faces without the sigma factor would produce significantly greater errors in R_W than the somewhat more blunted, but much smaller in surface area, corners and edges.

The ringing artifacts in these last examples are somewhat analogous in scale to the texture or surface roughness of real-shaped rock and powder particles. Both texture information and ringing are contained in the higher-frequency terms of the SH expansion, so numerical methods for reducing ringing will also tend to smooth out the particle's real texture.

To conclude this section, Fig. 8 shows shape factors computed for axially symmetric ellipsoids with aspect ratios ranging from 0.01 (very oblate) to 100 (very prolate). In these plots, the open symbols joined by lines were obtained using the exact equations for the ellipsoid surface, principal curvatures, and normal vectors. Filled symbols were obtained using the SH series approximation for the ellipsoid with cutoff degree $N = 30$ and 150^2 Gaussian quadrature points.

As expected, all the sphericity and roundness factors have a maximum for a sphere (aspect ratio 1.0). Denoting the aspect ratio by α, the factor S_{BS} given by Eq. (3) has the property $S_{BS}(\alpha) = S_{BS}(\alpha^{-1})$, and its plot is steeper than the other sphericity factors, indicating that it might discriminate better among ellipsoids. For an ellipsoid of revolution, the factor S_{BS} is just equal to α or its reciprocal (i.e., the ratio of the smaller axis to the larger axis), which explains the symmetry in S_{BS}. This relationship also is approximately valid for R_n in Eq. (15), but none of the other plotted shape factors exhibit this property even approximately. The Hofmann shape entropy (S_H) in particular is much less sensitive to shape at smaller aspect ratios than for larger ones. Notice that the calculations using an SH series approximation for the ellipsoid surface (the filled symbols) are accurate to ≤ 5 % for all shape factors at all aspect ratios plotted. Therefore, we may be confident that the numerical procedures used here in conjunction with truncated SH approximations of particle shapes will yield shape factors that have similarly small errors.

3.2. Application to Real Particles

Seven different sources of particles were examined in this study and are described in Table II.[3] These seven were selected because of their widely differing mineralogy and size ranges, so we expect the results of this study to be generally applicable to many types of particles commonly encountered in engineering applications. The size ranges reported in the table, which can be defined in many ways for random-shape particles [24], were defined by measurement with ASTM standard sieves. The values of L/W and W/T, averaged over all particles in a given source, are reported in Table II to give some idea of shape differences among particle sources.

As described already, the sedimentary geology community uses the triaxial dimensions D_1, D_2, D_3 to characterize the overall shape of a particle using macroscopic shape factors. The definitions of D_2 and D_3 are quite similar to the definitions of W and T, respectively, used by the construction aggregate community, so it is useful to compare values of D_2 and W (Fig. 9), and of D_3 and T (Fig. 10) for a variety of real particles. These figures show that, for 3131 particles sampled at random from the first six sources sources described in Table II, D_2 and D_3 are nearly identical to W and T, respectively. The linear regression models of the data are shown in the figures. Each one has a slope of nearly one, and intercept of nearly zero, and a coefficient of determination, R^2 exceeding 0.99. Moreover, if we classify the data into the micrometer-size cement and the millimeter-sized aggregate particles, the results for each size class are not greatly different than the those shown in the plots. The slopes for D_2 vs. W are 0.991 and 0.995 for the cement and aggregate classes, respectively, and the R^2 values both exceed 0.995. The differences among size classes are slightly more pronounced for D_3 vs. T, with the slopes being 0.987 and 1.003 and the R^2 values being

[3]Some materials and manufacturers are identified to make the procedures clear. Such identification does not imply recommendation or endorsement by the National Institute of Standards and Technology (NIST), nor does it imply that the materials identified are necessarily the best available for the purpose.

0.987 and 0.999 for the cement and aggregate classes, respectively.

To be more rigorous about the statistical differences between D_2 and W, a paired t-test was performed on the normalized quantity $(W - D_2)/W$. The paired t-test produced a 95 % confidence interval of $(0.0056, 0.0065)$ for the mean value of $(W - D_2)/W$. In other words, in 95 % of random samples from this population of particles, W will exceed D_2 by about 0.6 % when averaged over the sample. The same analysis on $(T - D_3)/T$ produced a 95 % confidence interval of $(-0.002, 0.000)$. Therefore, we conclude that the sets $\{L, W, T\}$ and $\{D_1, D_2, D_3\}$ are nearly equal within statistical, measurement, and computational uncertainty, and for practical purposes these two sets can be used interchangeably to compute common shape factors describing sphericity [10, 11, 12, 13, 3].

The radii ρ_{is} and ρ_{es} of the bounding spheres were calculated for all 3131 particles from the first six particle sources. One might expect that (a) the diameter of the minimum enclosing sphere is equal to, or at least strongly correlated with L (or D_1), and (b) the maximum inscribed sphere diameter might equal or be strongly correlated with T. Fig. 11 plots T vs. $2\rho_{\text{is}}$ and L vs. $2\rho_{\text{es}}$ for the 3131 particles sampled in this investigation. As expected, L and $2\rho_{\text{es}}$ are very nearly equal over a wide range of sizes and shapes. However, T tends to be modestly greater than $2\rho_{\text{is}}$; in fact, no particle was found for which $T < 2\rho_{\text{is}}$. T is the largest axis perpendicular to both L and W, so either or both of the opposite surface points defining T can easily be outward protrusions on the particle surface and thus lie outside the maximum inscribed sphere. But the maximum inscribed sphere is considerably more constrained because it must lie entirely within the particle, and so will be influenced by inward protrusions instead of outward ones. Therefore, it is reasonable that $T \geq 2\rho_{\text{is}}$.

This relationship between the diameter of the bounding sphere and L is further explored using the seventh particle source in Table II. A previous paper [25] examined particles from a single quarry, which had all been blasted and crushed, but with particle sizes ranging from 20 μm to 38 mm as measured by ASTM standard sieves. Various measures of shape were compared among broad size classes that together spanned the entire sieve size range. In this present work, three size classes of those same particles were compared in terms of the sphericity factors defined in this paper: S_H, S_W, and S_{BS}, as well as a measure of the difference between L and $2\rho_{\rm es}$ and between T and $2\rho_{\rm is}$. S_H values were calculated using the $\{L, W, T\}$ dimensions. All five quantities were compared among three size classes, as determined by sieve analysis, to further check how, if at all, the particle shape is affected by particle size. Table III contains the results for the three size classes, covering a total range of 1180 μm to 20 μm. Based on the columns for S_H, S_W, and S_{BS}, the two larger size ranges have almost identical sphericity factors. The smallest size range of particles gives results that are equal to within the standard deviation, but the average values are lower, indicating that perhaps the smallest particles are a little less like spheres than are the larger particles.

The dimension ratios $T/2\rho_{\rm is}$ and $L/2\rho_{\rm es}$ were calculated for all the particles in each size class, and the averages and standard deviations computed. Table 3 shows for both ratios that the average values and standard deviations are nearly the same for all three size classes, so these measures of shape appear to have a universal scaling. The average value of $L/2\rho_{\rm es}$ plus or minus one standard deviation covers the value of one, indicating that L and the the diameter of the minimum enclosing sphere often may be equal, at least for these particles.

Is this apparent equality between L and $2\rho_{\rm es}$ generally true for star-shaped particles? It cannot be true for all star-shaped particles, as we show next. In 2D, consider an equilateral triangle, which is not only star-shaped but also convex. Its longest dimension is the length L of one of the sides, so that the L axis is totally contained in the surface. But the minimum enclosing circle for an equilateral triangle touches all three vertices and has a radius of $\rho_{\text{es}} = L/\sqrt{3}$ (i.e., a diameter of $2\rho_{\text{es}} = 2L\sqrt{3}/3$), so that $2\rho_{\text{es}} > L$. In 3D, a regular tetrahedron (*i.e.*, one with equilateral triangular faces) with edge length L has an enclosing sphere with diameter $\rho_{\text{es}} = \sqrt{6}L/2$ and L is clearly the maximum dimension, so again $2\rho_{\text{es}} > L$. In fact, we can prove by contradiction that generally L is a lower bound to the diameter of the maximum enclosing sphere. Suppose that L is *not* a lower bound for the diameter $2\rho_{\text{es}}$ of the bounding sphere of a given star-shaped particle, so that $2\rho_{\text{es}} < L$. But the diameter of a sphere is, by definition, the length of the longest line segment that the sphere can contain. Therefore, the bounding sphere cannot completely contain L and so at least one of the two endpoints defining L. But both endpoints of L lie on the particle surface, so at least part of the particle surface lies outside the sphere. Therefore, the given sphere is not the bounding sphere, so we have reached a contradiction. Therefore we have proved that $L \leq 2\rho_{\text{es}}$.

In a similar manner, we can prove by contradiction that T is an upper bound on the diameter of the maximum inscribed sphere, that is $T \geq 2\rho_{\text{is}}$. Suppose instead that $2\rho_{\text{is}} > T$. A diameter of the maximum inscribed sphere, having length $2\rho_{\text{is}}$, can be constructed through that sphere's center at any orientation. In particular, such a diameter can be constructed that is coplanar with and parallel to the T axis. But this particular diameter, like T, is necessarily perpendicular to both L and W, in which case we have found a line segment wholly within the particle that is longer than T and is perpendicular to both L and W. Consequently, T cannot be the thickness dimension of the particle, and we have reached a contradiction. Therefore, $T \geq 2\rho_{\text{is}}$.

One might think that $L/2\rho_{\text{es}}$ or $T/2\rho_{\text{is}}$ could be defined as another shape parameter. However, neither would be useful because both would have the same value, one, for any triaxial ellipsoid including a sphere. For all these shapes, for example, T coincides with the diameter of the maximum inscribed sphere and both are equal to the smallest of the three axes.

Figs. 12 and 13 show respectively the mean values of the Wadell sphericity, S_W, according to Eq. (2), and the mean values of Hofmann's shape entropy factor, S_H, in Eq. (4). Neither of these factors significantly distinguishes one source from another. The mean values of S_W among the different sources differ by no more than 0.04, which is small compared to the variation of about 0.16 within each source. S_H has only slightly better sensitivity than S_W, with mean values among different sources differing by only about 0.032, but with a smaller within-source variation of about 0.05. These low sensitivities are not too surprising considering that $S_H \geq 0.99$ for all five platonic solids in Table I.

Further examination of Table I suggests that S_{BS} might be a more sensitive indicator of how equiaxed a particle is, because it has a greater range of values for these simple geometric shapes. Fig. 14 shows the mean values of S_{BS} for the same six particle sources. As expected, the variation in the mean values is about 0.12, somewhat greater than for either S_W or S_H, although the within-source variation is also greater, up to 0.20. In addition, based on a visual comparison of the three fine aggregate sources in Fig. 15, S_{BS} qualitatively appears to differentiate the sphericity of the three fine aggregate sources more faithfully ($FA3 < FA1 \approx FA2$) than does S_W, the latter indicating that all three have about the same sphericity.

Fig. 16 illustrates the distribution of local roundness, measured as R_W, for three different particles: a cuboid formed by truncating the SH approximation of a cube at $N = 30$, and one specimen each of CA1 and FA1 aggregates. Also depicted in the figure are the calculated values of S_W, R_W, and R_n. These images provide a clear indication of the fidelity with which these three factors reflect the qualitative notions of sphericity and roundness. For example, the CA1 particle has significantly lower calculated sphericity than the other two particles, while the cuboid and FA1 particle have similar sphericities, with the FA1 particle being modestly more spherical.

This relative ranking seems reasonable upon visual comparison of the particles. The roundnesses, however, as measured by R_W, seem to compare poorly to the images. For example, the cuboid has R_W significantly lower than either the CA1 or the FA1 particle, the latter two having almost identical values of R_W. But visual comparison of the particles suggests that the FA1 particle is more rounded than the CA1 particle; the CA1 particle has sharp, knife-like edges along its surface, but the FA1 particle appears to have significantly blunter edges. In fact, R_n appears to be a superior measure of roundness, as it ranks both the cuboid and the FA1 particle as much more rounded than the CA1 particle.

Passing now to the statistical distribution of R_W and of R_n among the six aggregate sources, Figs. 17 and 18 show the mean values of these roundness factors. Again, for the fine aggregates, mean values of R_n appear to rank the sources more reasonably than R_W. The photographic evidence in Fig. 15 suggests that the FA3 source is more angular than either FA1 or FA2, the latter two sources appearing qualitatively similar in roundness. R_n captures this ranking, but R_W would indicate that FA1 and FA3 have nearly the same roundness, with FA2 being ranked significantly lower than any of the other five aggregate sources.

4. Conclusions

Truncated SH approximations of star-shaped particles provide a convenient means to quantitatively analyze the shape. This study examined the ability of the SH approximation method to accurately calculate macroscopic quantities such as triaxial dimensions and the bounding spheres. An examination of the five Platonic solids, of a wide range of ellipsoids, and of 3131 particles coming from six different real sources demonstrated that the triaxial dimensions $\{D_1, D_2, D_3\}$ commonly used by sedimentary geologists are essentially identical to the set $\{L, W, T\}$ used in the construction aggregate industry. Furthermore, we proved that L is a lower bound on the diameter of the particle's minimum enclosing sphere, although for most random shape particles these two quantities are very nearly equal. Similarly, we have proven that T is an upper bound on the diameter of the particle's maximum inscribed sphere.

The distribution of principal curvatures on the surface of star-shaped particles also can be calculated from the SH series approximation of the shape. Both artificial ringing, due to the truncation of the SH series, and real texture of the particle surface, can introduce considerable noise in the distribution of curvatures. This noise can be reduced significantly by application of Lanczos's sigma factor, although at the probable price of removing some real surface detail along with the noise.

Both macroscopic parameters and surface integrals of differential quantities can be used to calculate shape factors describing sphericity or roundness. We examined three sphericity factors in detail: S_W, the true sphericity, S_{BS} , the radius ratio of the bounding spheres, and the Hofmann shape entropy, S_H. In addition, we examined two factors to describe roundness. The first of these, R_W, is a 3D generalization of the roundness factor originally introduced by Wadell. The second roundness factor, which to our knowledge is used here for the first time, is a surface integral of the dot product of the unit position vector with the unit normal vector. A comparison of these two roundness factors for six sources of real particles indicated that R_n more faithfully captures our common visual perception of roundness. Furthermore, R_n is considerably easier to calculate numerically than R_W, because it does not require either foreknowledge of the maximum inscribed sphere radius or a calculation of the distribution of principal curvatures over the surface. A seventh source of real rock particles, subjected to a combination of blasting and crushing operations and classified into three size classes, showed that the various sphericity and roundness factors are essentially size invariant for this material.

Acknowledgment

The authors are grateful to Joseph Main, Timothy Hall, and Kenneth Snyder for helpful discussions and thoughtful reviews of the manuscript. We thank Will Guthrie for his help with the statistical analysis of particle dimensions. Partial support of this work was provided by the National Institute of Standards and Technology Project: Innovative Measurement Science–Shape Metrology.

References

[1] J. F. Douglas, E. J. Garboczi, Intrinsic viscosity and the polarizability of particles having a wide range of shapes, Adv. Chem. Phys. 91 (1995) 85–153.

[2] J. Bicerano, J. F. Douglas, D. A. Brune, Model for the viscosity of particle dispersions, J. Macromol. Sci., Rev. Macromol. Chem. Phys. C39 (4) (1999) 561–642.

[3] J. P. Le Roux, Comparison of sphericity indices as related to the hydraulic equivalence of settling grains, J. Sedimentary Petrology 67 (3) (1997) 527–530.

[4] J. P. Le Roux, Application of Hofmann shape entropy to determine the settling velocity of irregular, semi-ellipsoidal grains, Sediment. Geol. 149 (2002) 237–243.

[5] E. J. Garboczi, K. A. Snyder, J. F. Douglas, M. F. Thorpe, Geometrical percolation threshold of overlapping ellipsoids, Phys. Rev. E 52 (1995) 819–828.

[6] S. Torquato, Random Heterogeneous Materials, Springer, New York, 2001.

[7] R. Weinstock, Calculus of Variations, Dover, New York, 1974.

[8] H. Wadell, Volume, shape, and roundness of rock particles, J. Geology 40 (5) (1932) 443–451.

[9] B. B. Mandelbrot, Fractals: Form, Chance and Dimension, W. H. Freeman & Company, New York, NY, 1977.

[10] A. T. Corey, Influence of shape on the fall velocity of sand grains, MSc thesis, Colorado A&M College, Fort Collins, Colorado (1949).

[11] E. D. Sneed, R. L. Folk, Pebbles in the lower Colorado River. Texas—a study in particle morphogenesis, J. Geology 66 (1958) 114–150.

[12] N. C. Janke, Effect of shape upon the settling velocity of regular convex geometric particles, J. Sedimentary Petrology 36 (1966) 370–376.

[13] H. J. Hofmann, Grain-shape indices and isometric graphs, J. Sediment. Res. A 64 (1994) 916–920.

[14] W. C. Krumbein, Measurement and geological significance of shape and roundness of sedimentary particles, J. Sediment. Petrol. 11 (2) (1941) 64–72.

[15] S. Rudduck, M.-A. Williams, Conceptual ternary diagrams for shape perception: A preliminary step, in: Proceedings of the 2010 AAAI Spring Symposium Series, 2010, pp. 34–38.

[16] C. M. Cooper, S. Testa, A quick method of determining rock surface area for quantification of the invertebrated community, Hydrobiologia 452 (2001) 203–208.

[17] ASTM Standard D4791-10, Standard Test Method for Flat Particles, Elongated Particles, or Flat and Elongated Particles in Coarse Aggregate, ASTM International, West Conshohocken, PA, DOI: 10.1520.D4791-10 (2010).

[18] M. A. Taylor, E. J. Garboczi, S. T. Erdoğan, D. W. Fowler, Some properties of irregular 3-D particles, Powder Technol. 162 (2006) 1–15.

[19] E. J. Garboczi, Three-dimensional mathematical analysis of particle shape using X-ray tomography and spherical harmonics: Application to aggregates used in concrete, Cem. Concr. Res. 32 (10) (2002) 1621–1638.

[20] E. J. Garboczi, J. W. Bullard, Shape analysis of a reference cement, Cem. Concr. Res. 34 (2004) 1933–1937.

[21] E. J. Garboczi, Three dimensional shape analysis of JSC-1A simulated lunar regolith particles, Powder Technol. 207 (2011) 96–103.

[22] C. Lanczos, Applied Analysis, Prentice Hall, Englewood Cliffs, NJ, 1956.

[23] E. Kreyszig, Differential Geometry, Dover, New York, 1991.

[24] S. T. Erdoğan, E. J. Garboczi, D. W. Fowler, Shape and size of microfine aggregates: X-ray microcomputed tomography vs. laser diffraction, Powder Technol. (177) 53–63.

[25] E. J. Garboczi, X. Liu, M. A. Taylor, The 3-D shape of blasted and crushed rocks: From 20 μm to 38 mm, Powder Technol. 229 (2012) 84–89.

List of Figures

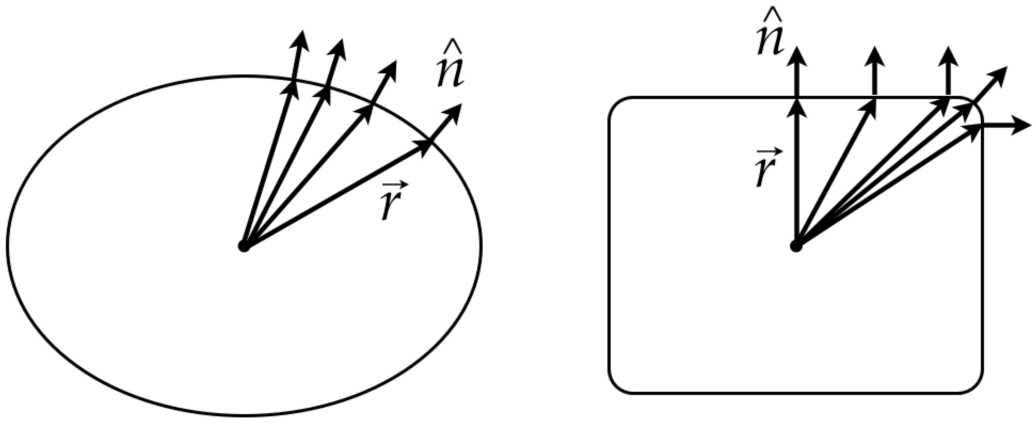

Figure 1: Illustration of how the angle between the position vector $\vec{r}$ and the unit normal $\hat{n}$ provide an indication of roundness. Regions visually associated with high angularity (i.e., two flat regions joined by a high-curvature region) correspond to large angles between $\vec{r}$ and $\hat{n}$.

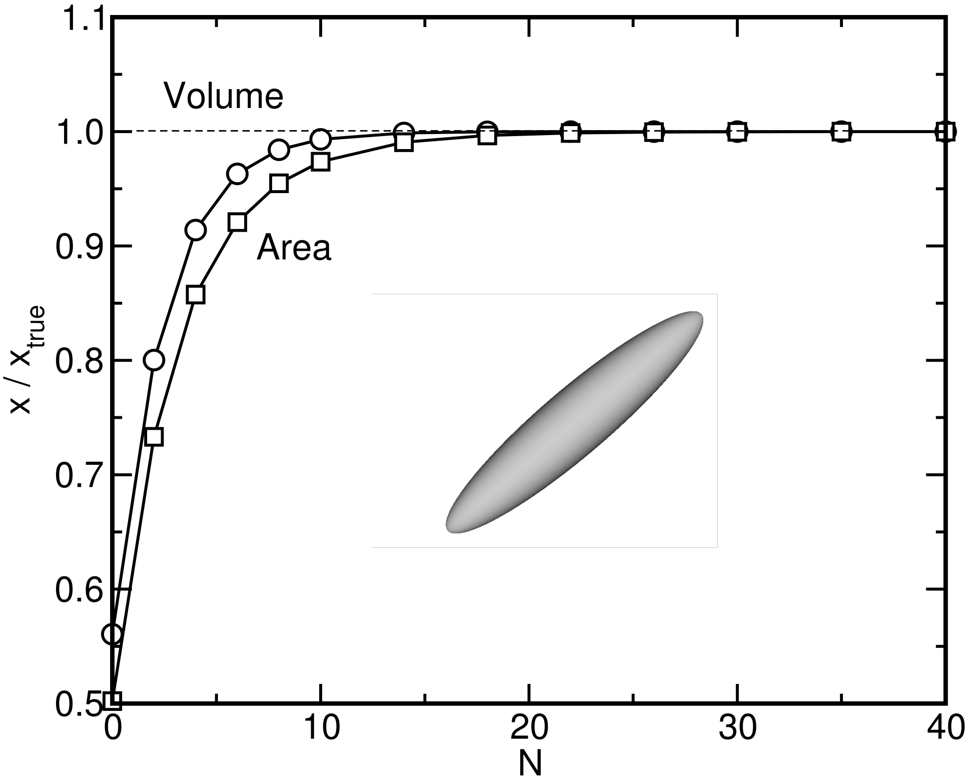

Figure 2: Calculated volume and surface area of a prolate 5:1 ellipsoid, normalized to their true values, as a function of the cutoff degree N of the SH expansion. All calculations used 150^2 Gaussian quadrature points, and the Lanczos sigma factor was not applied.

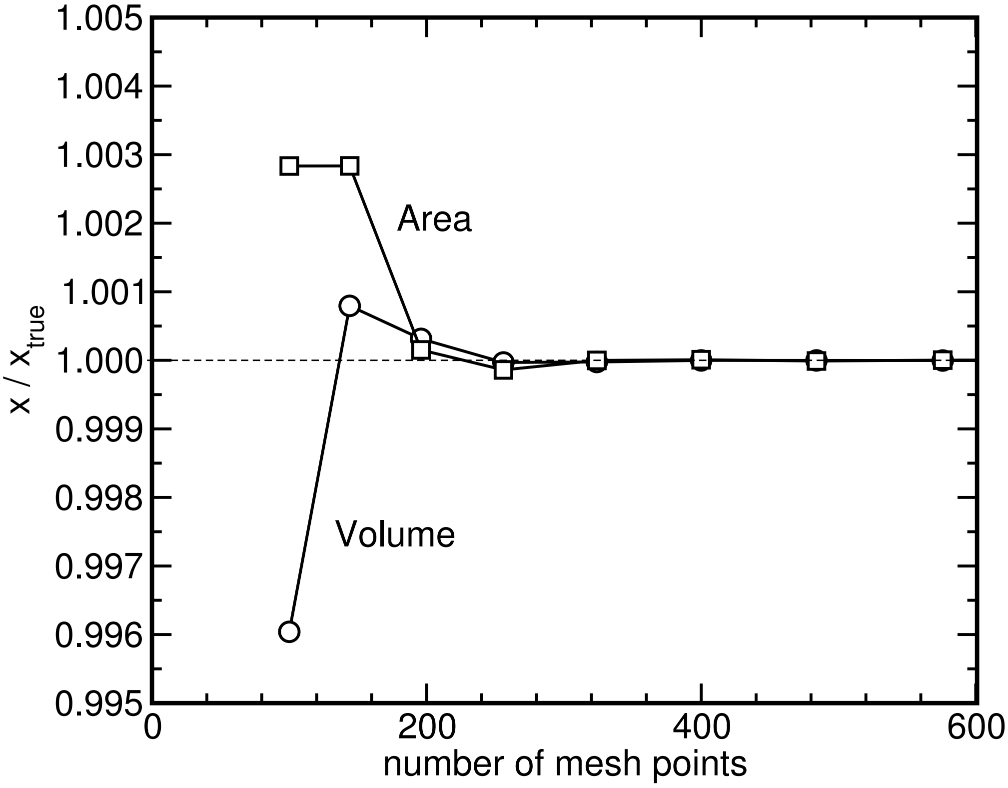

Figure 3: Calculated volume and surface area of a prolate 5:1 ellipsoid, normalized to their true values, as a function of the number of Gaussian quadrature points. All calculations used a cutoff degree $N = 60$, and the Lanczos sigma factor was not applied.

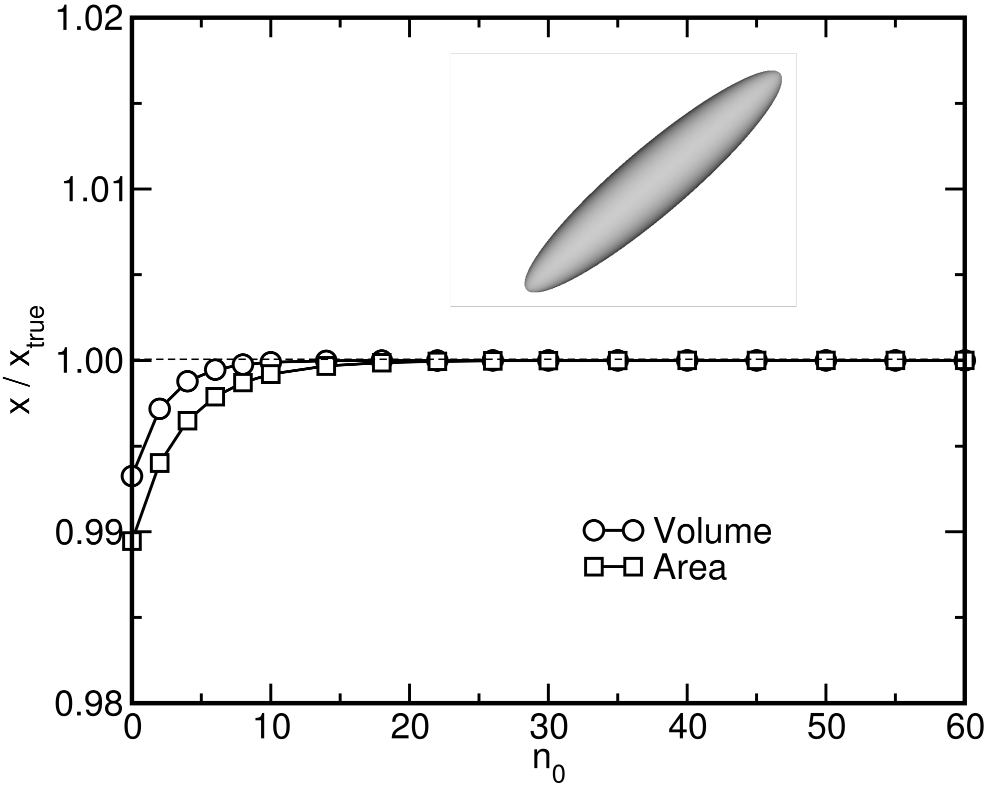

Figure 4: Influence of Lanczos sigma factor on calculated volume and surface area of a prolate 5:1 ellipsoid. Values are plotted against the degree n_0 at which the sigma factor begins to be applied. All calculations used a cutoff degree $N = 60$ and 150^2 Gaussian quadrature points.

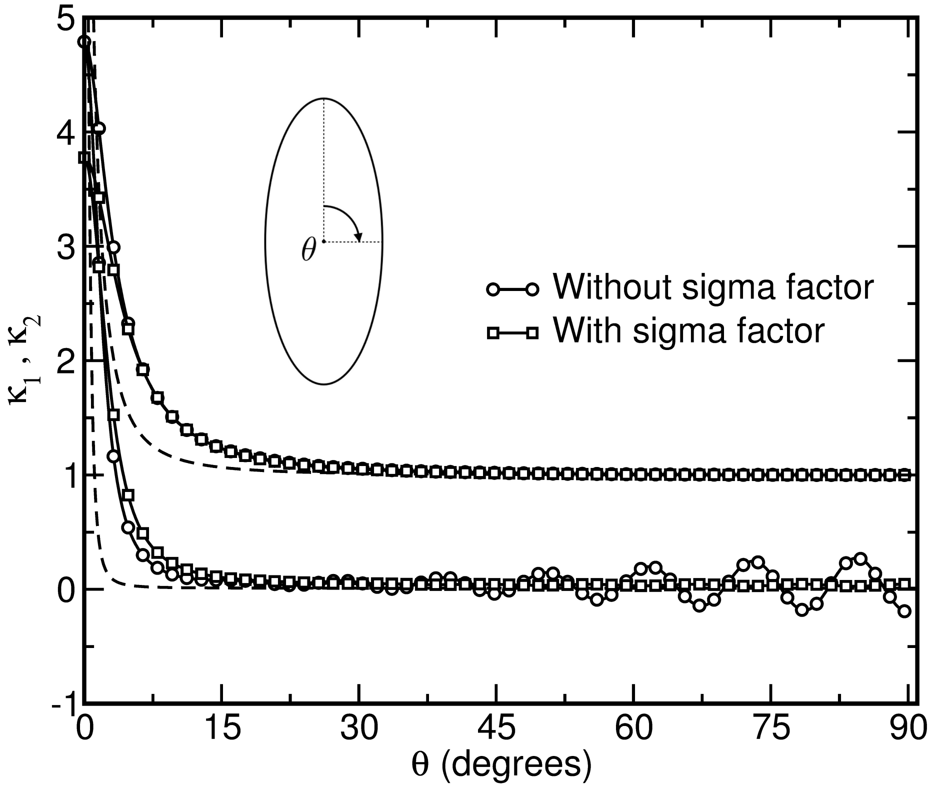

Figure 5: Calculated principal curvatures of a 5:1 prolate ellipsoid along a constant-ϕ path from $\theta = 0°$ to $\theta = 90°$. Values calculated without (circles) and with (squares) the application of the Lanczos sigma factor to reduce the effects of ringing. The SH expansion was truncated at $N = 30$. Dashed curves are the calculated principal curvatures using the exact equation for the ellipsoid.

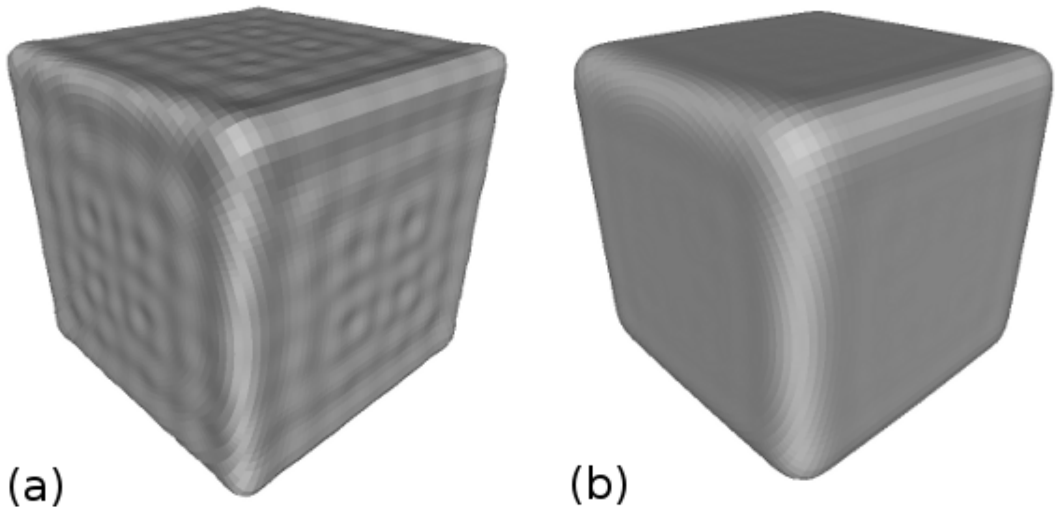

Figure 6: Calculated shape of a cube (a) without and (b) with the Lanczos sigma factor applied. Both images were created with $N = 30$ and using 150^2 points on the surface.

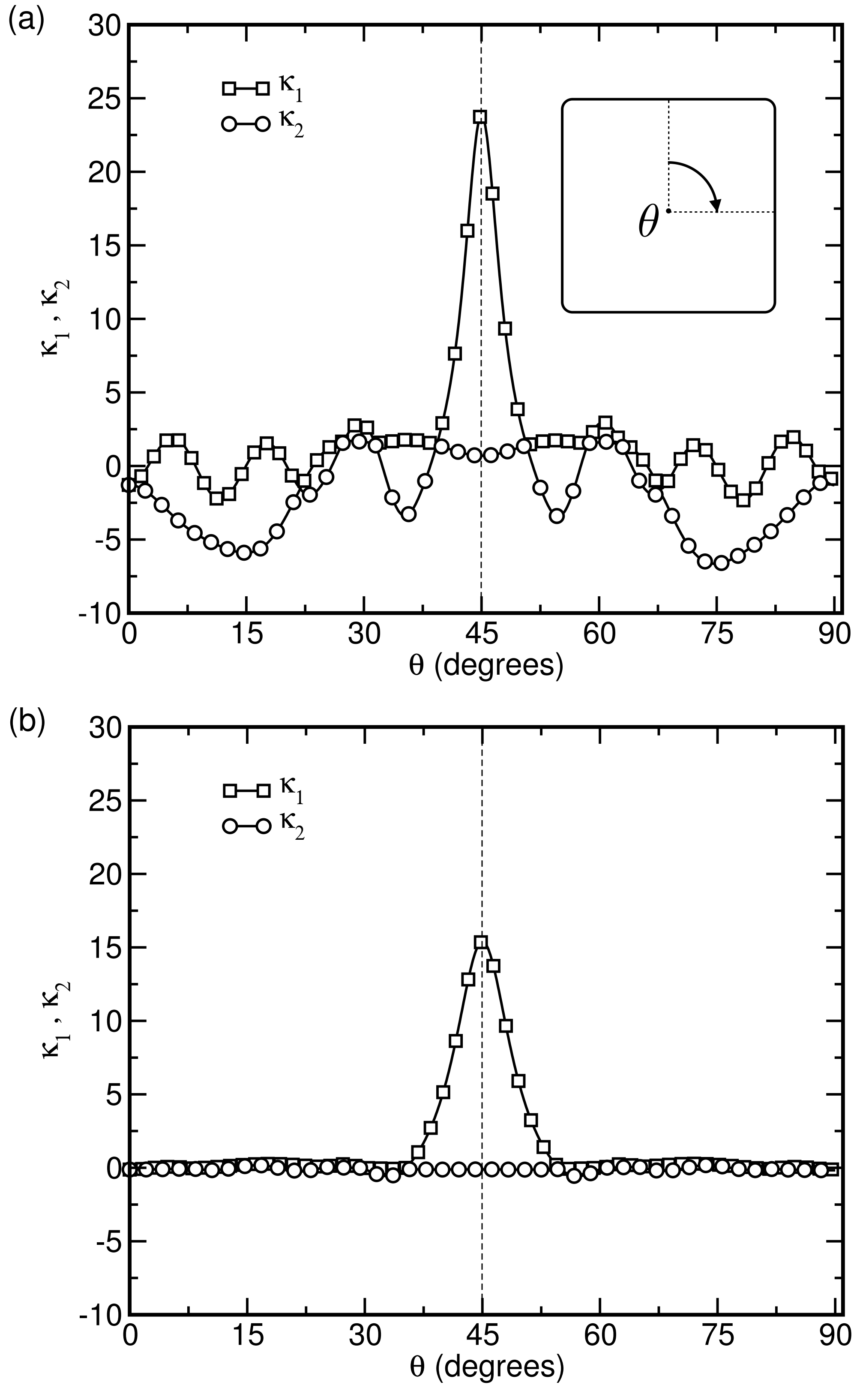

Figure 7: Calculated principal curvatures of a cube along a constant-ϕ path from $\theta = 0°$ to $\theta = 90°$. Values calculated (a) without and (b) with the application of the Lanczos sigma factor to reduce the effects of ringing. The SH expansion was truncated at $N = 30$.

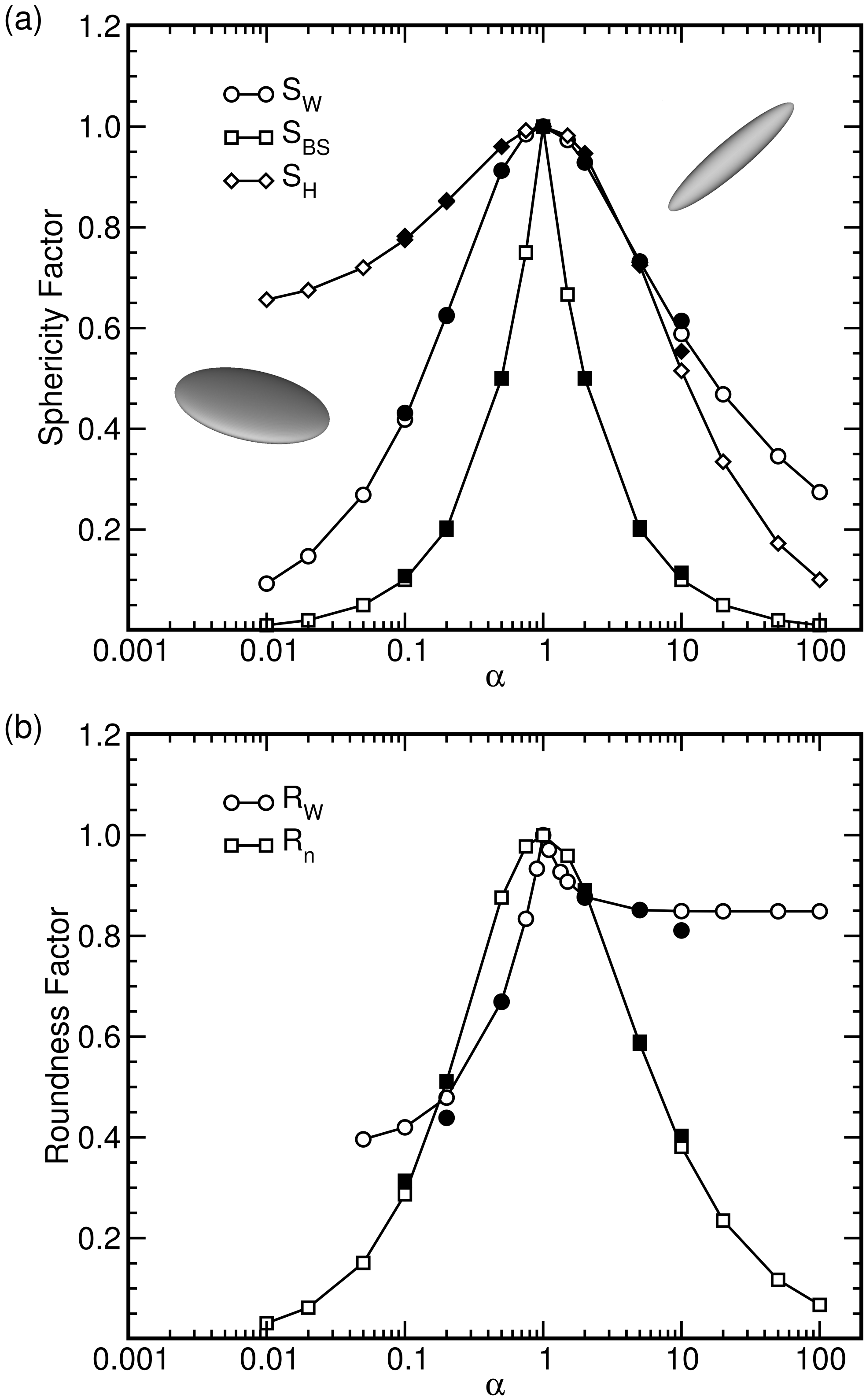

Figure 8: Shape factors for (a) sphericity and (b) roundness computed for axially symmetric ellipsoids as a function of aspect ratio c/a. Open symbols joined by lines use the analytic equations for the ellipsoid surface, curvatures, and normal vectors, although integration was performed numerically. Filled symbols are for the SH approximation of the ellipsoid with $N = 30$ and 150^2 quadrature points.

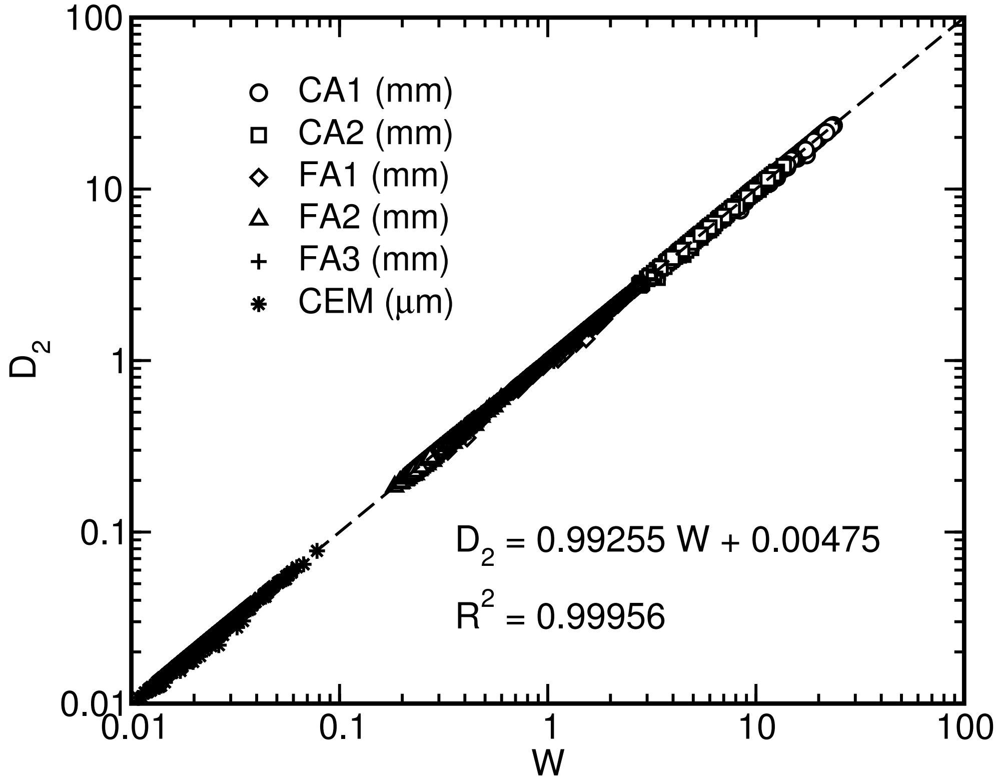

Figure 9: Comparison of particle width to the triaxial dimension D_2 for 3131 particles spanning six different sources. Dashed line is the identity line.

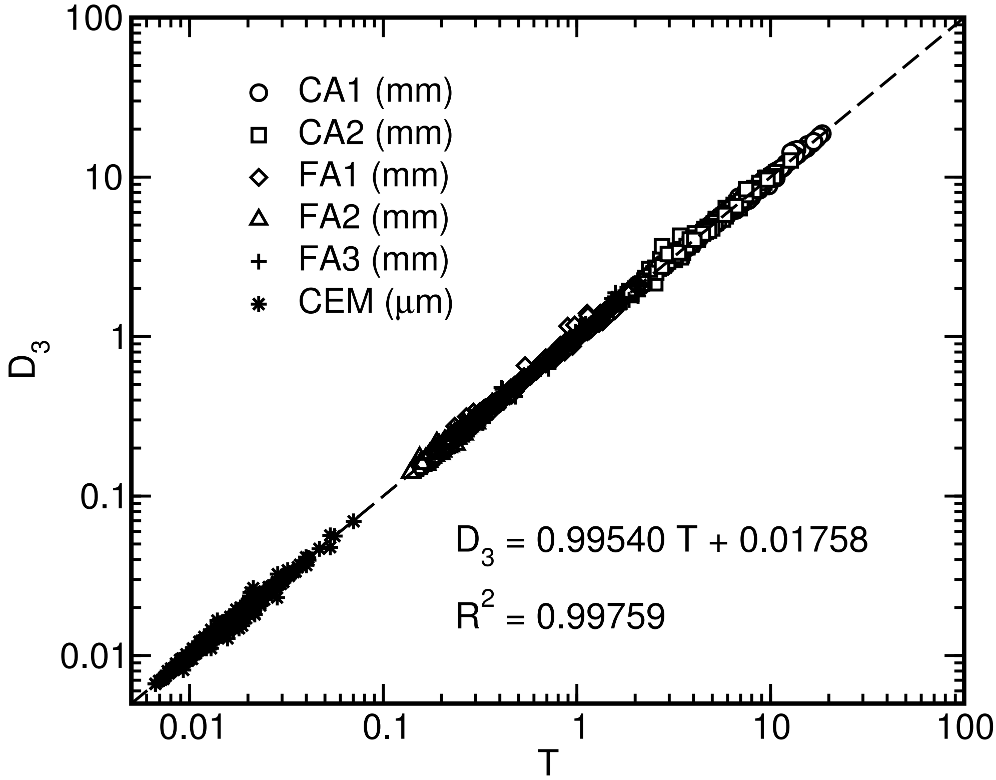

Figure 10: Comparison of particle thickness to the triaxial dimension D_3 for 3131 particles spanning six different sources. Dashed line is the identity line.

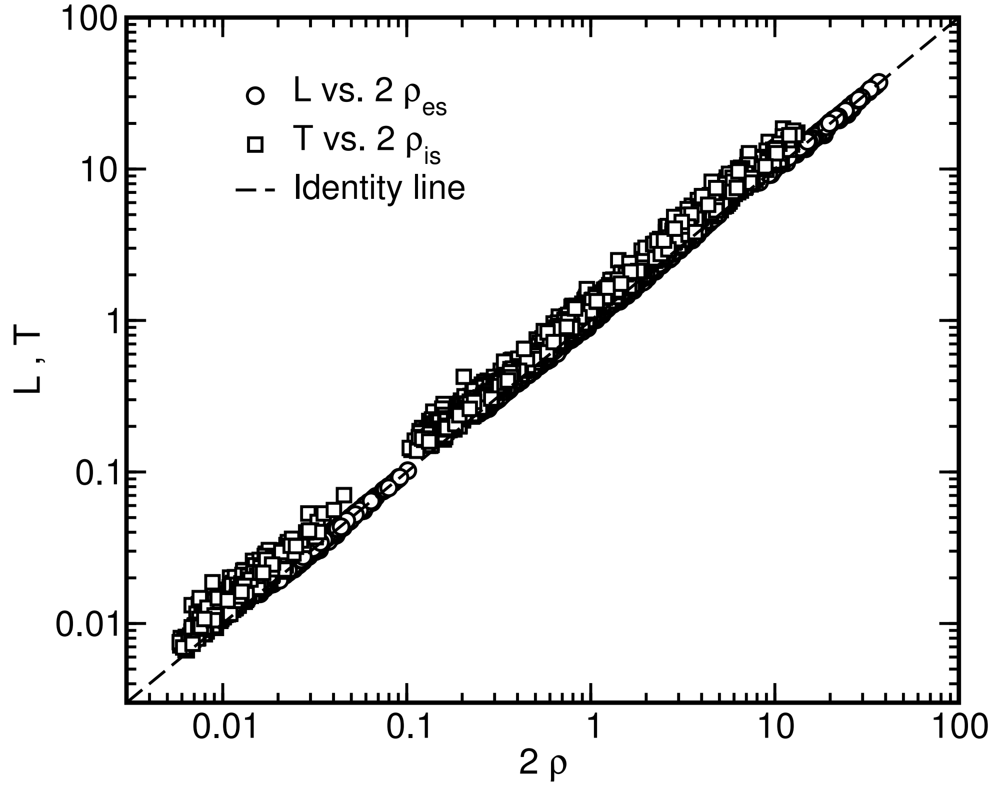

Figure 11: Comparison of the correlation between $2\rho_{\rm es}$ and D_1, and between $2\rho_{\rm is}$ and D_3. Dashed line is the identity line.

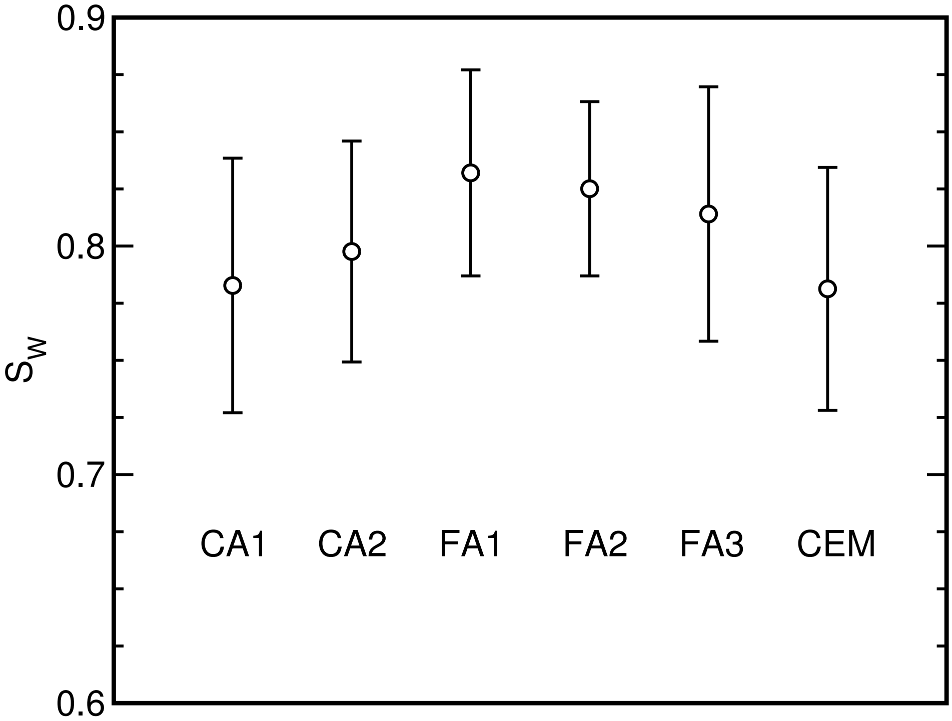

Figure 12: Mean value of S_W for the first six particle sets described in Table II. Vertical bars represent ± 1 sample standard deviation.

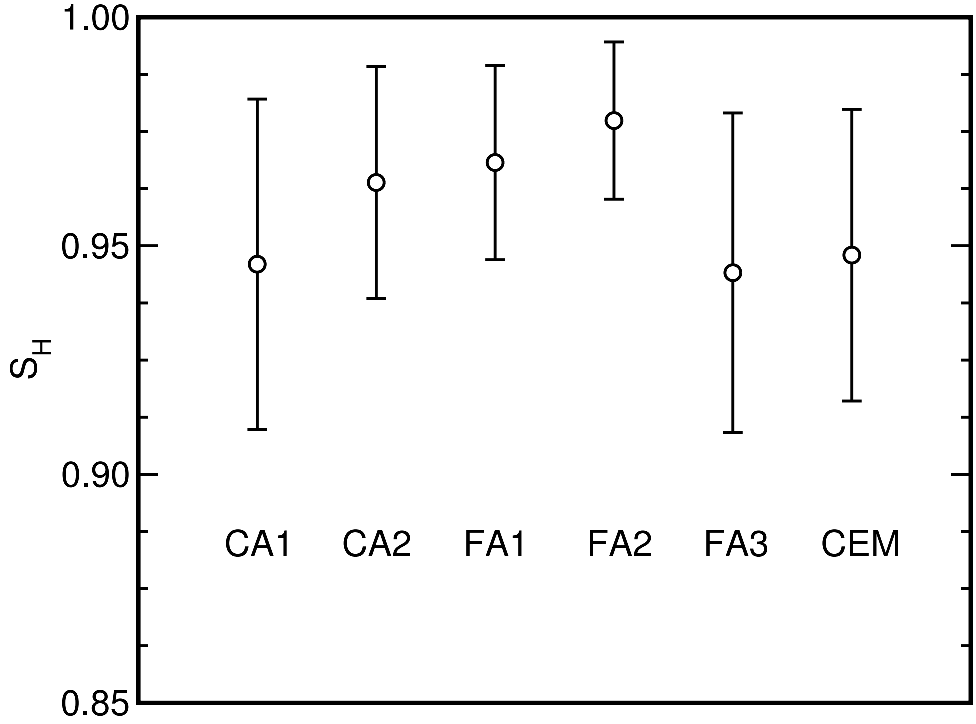

Figure 13: Mean value of S_H, as defined by Eq. (4), for the first six particle sets described in Table II. Vertical bars represent ±1 sample standard deviation.

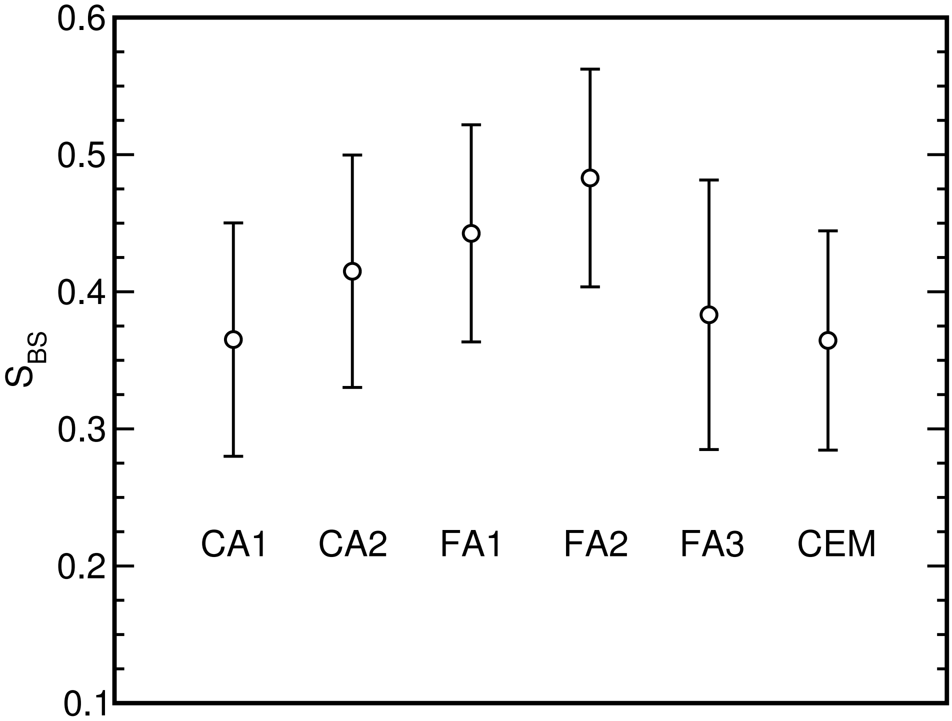

Figure 14: Mean value of S_{BS} for the first six particle sets described in Table II. Vertical bars represent ± 1 sample standard deviation.

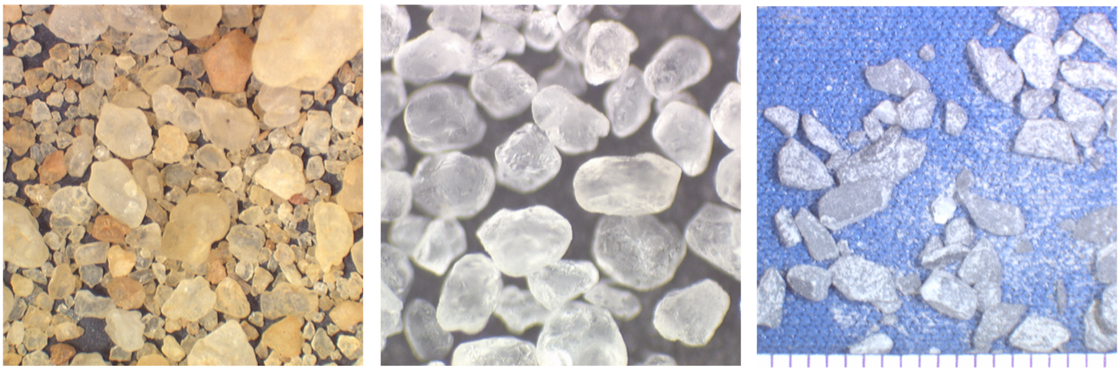

FA1 FA2 FA3

Figure 15: Photographs of the three sources of fine aggregate (sand) used in this investigation.

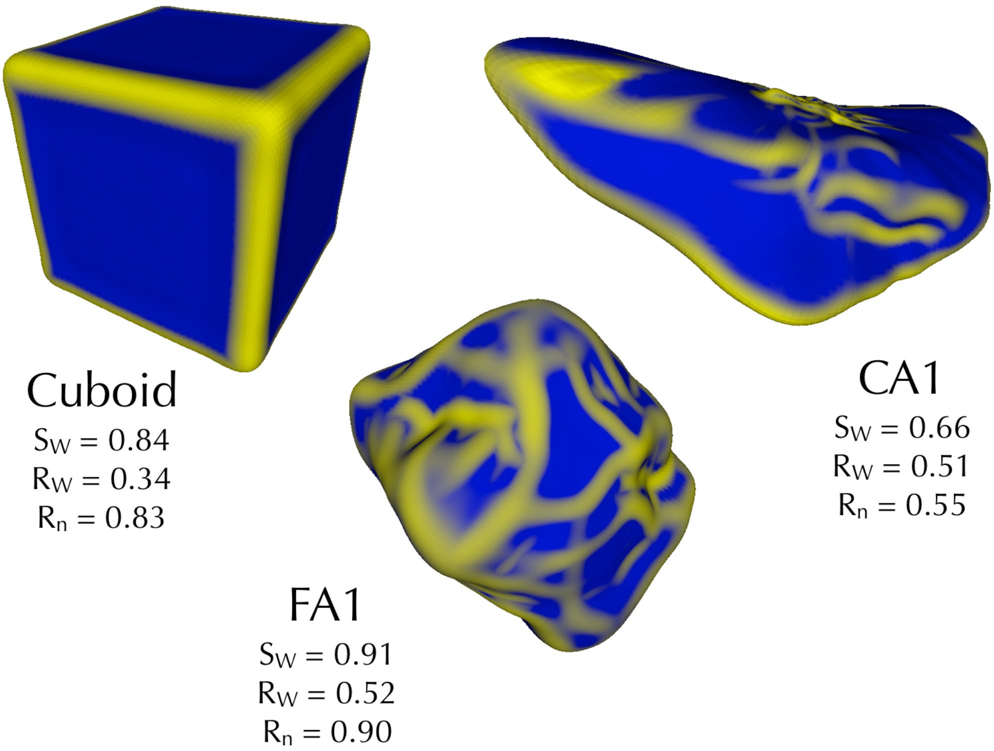

Figure 16: Local distribution of R_W using the kernel of Eq. (12) for a cube, a CA1 particle, and an FA1 particle. In each case, the SH cutoff degree $N = 30$ and the Lanczos sigma factor was applied starting at degree 10. Bright regions on the particle surface are those that have greater values of the kernel of Eq. (12).

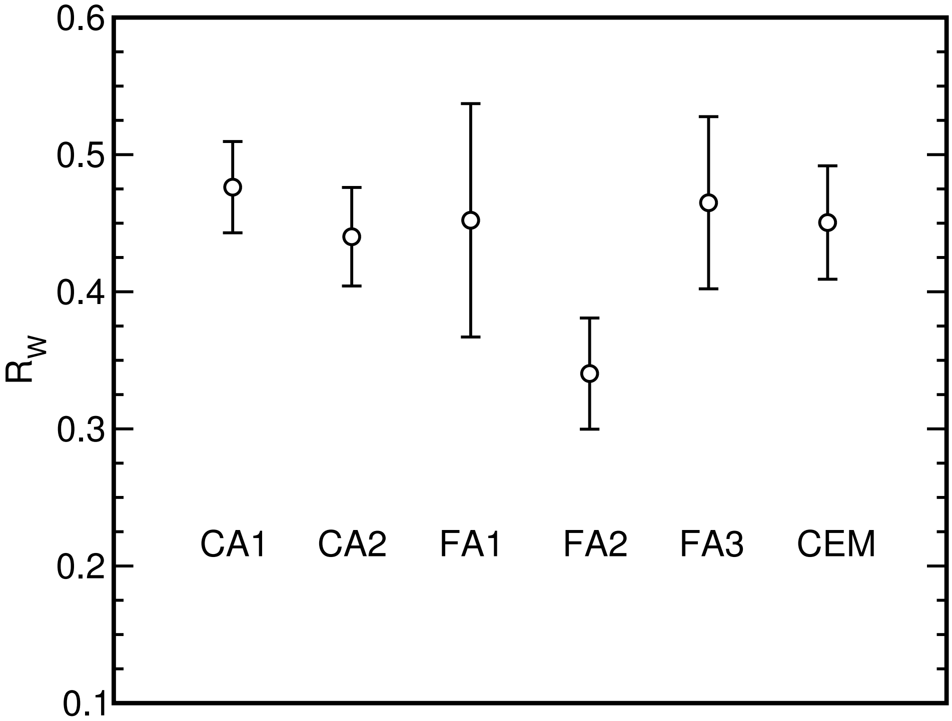

Figure 17: Mean value of R_W, as defined by Eqs. (12) and (13), for the first six particle sets described in Table II. Vertical bars represent ± 1 sample standard deviation.

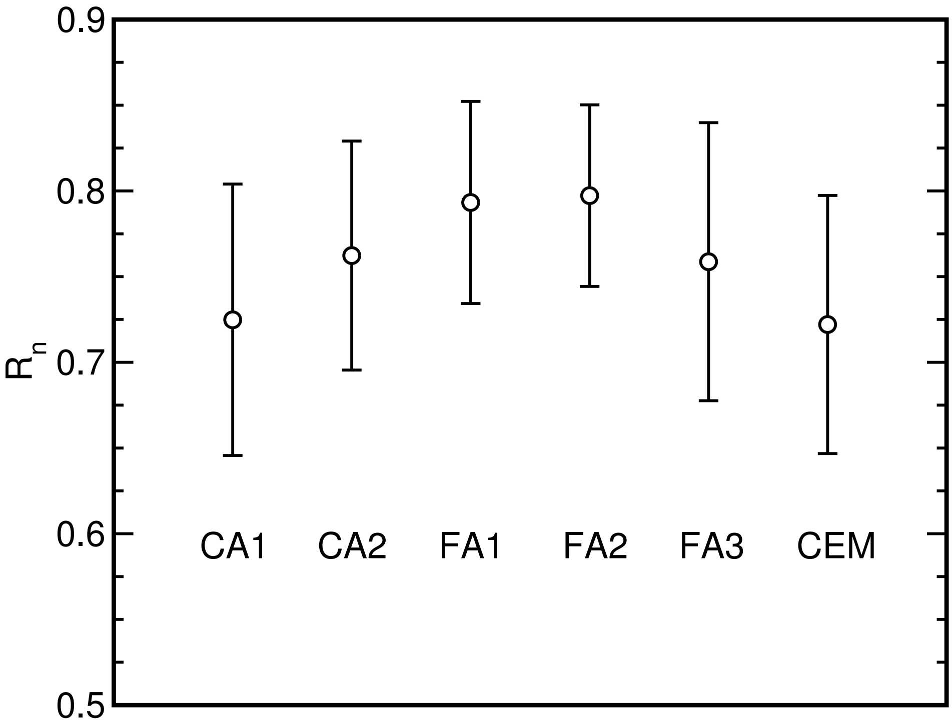

Figure 18: Mean value of R_n, as defined by Eq. (15) for the first six particle sets described in Table II. Vertical bars represent ± 1 sample standard deviation.

List of Tables

Table 1: Shape and sphericity, as measured by S_W, S_{BS} and S_H of prolate ellipsoids and the five platonic solids.

Solid	Image	S_W	S_{BS}	S_H
Prolate Ellipsoid (10:1)	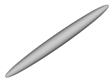	0.418	0.100	0.775
Prolate Ellipsoid (5:1)	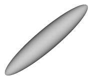	0.625	0.200	0.851
Tetrahedron	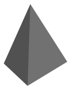	0.671	0.333	0.989
Cube	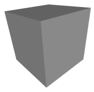	0.806	0.577	0.994
Octahedron		0.846	0.577	0.998
Dodecahedron		0.910	0.795	0.997
Icosahedron		0.939	0.795	0.997

Table 2: Description of the particle sources examined. In concrete and asphalt technology, gravel is called "coarse aggregate" (CA) and sand is called "fine aggregate" (FA).

Name	Description
CA1	Crushed coarse limestone aggregate produced by the American Association of State Highway Transportation Officials (AASHTO) as proficiency samples 137,138. Size range 8 mm to 40 mm. $\langle L/W \rangle = 1.47$ and $\langle W/T \rangle = 1.63$ (207 particles sampled).
CA2	Crushed coarse steel slag aggregate produced by Bethlehem Steel Co. plant in Sparrows Point, Maryland. Size range 4 mm to 25 mm. $\langle L/W \rangle = 1.38$ and $\langle W/T \rangle = 1.44$ (238 particles sampled).
FA1	Naturally rounded, nearly pure quartz sand (Ottawa sand) produced by U.S. Silica in Ottawa, Illinois. Size range 0.5 mm to 5 mm. $\langle L/W \rangle = 1.37$ and $\langle W/T \rangle = 1.39$ (615 particles sampled).
FA2	Fine rounded siliceous sand. Size range 0.2 mm to 1 mm. $\langle L/W \rangle = 1.31$ and $\langle W/T \rangle = 1.29$ (567 particles sampled).
FA3	Crushed fine aggregate for hot asphalt applications, produced by AASHTO as proficiency sample 39. Size range 0.5 mm to 5 mm. $\langle L/W \rangle = 1.47$ and $\langle W/T \rangle = 1.65$ (532 particles sampled).
CEM	Type I portland cement produced by the Cement and Concrete Reference Laboratory (CCRL) as proficiency sample 152. Size range 0.5 μm to 100 μm. $\langle L/W \rangle = 1.45$ and $\langle W/T \rangle = 1.61$ (972 particles sampled).
WIL	Blasted and crushed particles from a single rock source, sieved in different size ranges. Size ranges sampled were from 20 μm to 1180 μm . $\langle L/W \rangle = 1.39$ and $\langle W/T \rangle = 1.53$. $38,705$ particles sampled.

Table 3: Comparison of sphericity factors and dimensional differences between L and $2\rho_{\mathrm{es}}$ and between T and $2\rho_{\mathrm{is}}$ for three size ranges of the WIL particles. Values in parentheses are the sample standard deviations, and Num is the number of particles analyzed in a given size class.

Size (μm)	**Num**	$\mathbf{S_H}$	$\mathbf{S_W}$	$\mathbf{S_{BS}}$	$\mathbf{T/2}\rho_{\mathrm{is}}$	$\mathbf{L/2}\rho_{\mathrm{es}}$
600–1180	320	0.964 (0.025)	0.807 (0.048)	0.419 (0.081)	1.246 (0.127)	0.988 (0.017)
150–300	15829	0.960 (0.029)	0.809 (0.046)	0.413 (0.089)	1.240 (0.119)	0.991 (0.016)
20–75	22556	0.950 (0.037)	0.788 (0.056)	0.379 (0.092)	1.251 (0.015)	0.990 (0.017)